Transition States in a Protein Environment – ONIOM QM:MM Modeling of Isopenicillin N Synthesis

Marcus Lundberg,[1] Tsutomu Kawatsu,[1] Thom Vreven,[2] Michael J. Frisch,[2] and Keiji Morokuma[1,*]

[1] *Fukui Institute for Fundamental Chemistry, Kyoto University, 34-4 Takano Nishihiraki-cho, Sakyo-ku, Kyoto 606-8103, Japan*

[2] *Gaussian, Inc., 340 Quinnipiac Street, Building 40, Wallingford, CT 06492*

Abstract. To highlight the role of the protein in metal enzyme catalysis, we optimize ONIOM QM:MM transition states and intermediates for the full reaction of the non-heme iron enzyme isopenicillin N synthase (IPNS). Optimizations of transition states in large protein systems are possible using our new geometry optimizer with quadratic coupling between the QM and MM regions. [Vreven, T. et. al., *Mol. Phys.* **2006**, *104*, 701–704]. To highlight the effect of the metal center, results from the protein model are compared to results from an active site model containing only the metal center and coordinating residues [Lundberg, M. et. al., *Biochemistry* **2008**, *47*, 1031–1042]. The analysis suggests that the main catalytic effect comes from the metal center, while the protein controls the reactivity to achieve high product specificity. As an example, hydrophobic residues align the valine substrate radical in a favorable conformation for thiazolidine ring closure and contribute to product selectivity and high stereospecificity. A low-barrier pathway for β-lactam formation is found where the proton required for heterolytic O–O bond cleavage comes directly from the valine N–H group of the substrate. The alternative mechanism, where the proton in O–O bond cleavage initially comes from an iron water ligand, can be disfavored by the electrostatic interactions with the surrounding protein. Explicit protein effects on transition states are typically 1–6 kcal/mol in the present enzyme, and can be understood by considering whether the transition state involves large movements of the substrate as well as whether it involves electron transfer.

* To whom correspondence should be addressed: E-mail: morokuma@fukui.kyoto-u.ac.jp, Telephone:+81-75-711-7843

1. Introduction

Transition-metal enzymes catalyze some of the most fundamental biochemical processes, and can serve as inspiration for novel biomimetic catalysts. From the latter perspective, it is important to understand how the metal center and the protein matrix separately contribute to the catalytic activity of the enzyme system. A well-established approach to clarify the catalytic power of enzymes is to compare rates for the same reaction in enzyme and solution. [1,2] This is not possible for most transition-metal enzymes because their activity is critically linked to the redox activity of the metal. An alternative approach, employed in this investigation, is to calculate reaction barriers in the protein environment and directly compare these to barriers obtained without protein environment and to experimental reaction rates.

In the present investigation, the catalytic mechanism of the non-heme iron enzyme isopenicillin N synthase (IPNS)[3,4] is analyzed using ONIOM(QM/MM), an integrated quantum mechanics:molecular mechanics (QM:MM) method.[5-8] In the present QM:MM model, the metal center, i.e., iron, iron ligands and substrate, is treated by density-functional theory (DFT), while the rest of the enzyme is treated by a classical force field. The two-layer approach is not only computationally efficient, but also makes it easier to separate effects from the metal center from those of the surrounding protein because they are described at different computational levels. To further highlight the effects of the protein, the ONIOM results are compared to results from a study where the protein was treated as a homogenous dielectric medium (active-site QM-only approach).[9] QM/MM methods can be considered as extensions of the active-site approach as they explicitly include the effects of the protein on geometry, electronic structure and energies. [10]

The most important feature of the investigation is the large number of fully optimized transition states in QM:MM models with several thousands of atoms. This is possible by the use of an advanced optimization algorithm, the "fully coupled macro/micro–iterative" optimization scheme. [11] In this method, the macro-iteration of the "macro/micro iteration" scheme [12] is modified by explicitly including the quadratic coupling of the QM region with the MM region, which significantly improves the geometry convergence for optimization of transition states and avoids restrictions common in standard schemes. The MM contributions to the Hessian are described using analytical second derivatives of the MM potentials. To avoid cubic scaling with system size, direct and linear scaling (FMM) methods for the MM contributions are used to make

this step feasible. The same optimization algorithm has previously been used to identify two transition states in mammalian glutathione peroxidase (GPx)[13] and a transition state for homolysis of the Co–C bond in methylmalonyl-CoA mutase.[14]

The ability to locate transition states makes it possible to see how the protein matrix affects the reaction coordinate and to quantify the effects on reaction rates. Optimization approaches are appropriate when there are no major changes in protein structure, but cannot describe major changes in protein conformation. Still, optimized transition states gives the best estimate of the reaction coordinate and are ideal starting points for calculations of enzymatic free energies, using e.g., quantum mechanical thermodynamic cycle perturbation (QTCP)[15] or QM/MM free-energy perturbation.[16]

Isopenicillin N synthase is a member of a family of mononuclear non-heme iron enzymes with a 2-His-1-carboxylate iron-binding motif.[17-19] It uses the four-electron oxidative power of O_2 to transform the tripeptide substrate δ-(L-α-aminoadipoyl)-L-cysteinyl-D-valine (ACV) to isopenicillin N (IPN). The proposed mechanism[20] fits into a general scheme for the oxygen-activated non-heme iron enzymes, with initial formation of a ferryl–oxo [Fe(IV)=O] intermediate that then acts as a powerful oxidant, see Scheme 1. The reaction starts when dioxygen binds to the high-spin[21] ferrous iron, which gives a ferric superoxo species[22] that activates the cysteine β-C–H bond leading to formation of an iron-bound peroxide.[23] According to the proposal in reference 20, the peroxide abstracts the valine N–H proton to generate the ferryl–oxo and a water molecule. At the same time, the nitrogen performs a nucleophilic attack on the cysteine β-carbon, which leads to formation of the four-membered β-lactam ring, see Scheme 2. This pathway, in the present paper called the "substrate donor" mechanism, could not be found in previous active-site modeling.[9,24] In the alternative "ligand donor" mechanism a water ligand provides the proton required for O–O bond cleavage, and the ferryl–oxo is formed before the β-lactam ring can close, see Scheme 2.[9] In the ligand donor mechanism, β-lactam ring closure is coupled to a separate proton transfer reaction from the substrate to the iron water ligand. In total, this leads to the same ferryl-oxo intermediate as in the substrate donor mechanism, see Scheme 2. From this intermediate, the high-valent iron species further oxidizes the substrate by activation of the strong valine β-C–H bond. This reaction produces a reactive substrate radical that attacks the thiolate, leading to formation of the five-membered thiazolidine ring and the completed IPN product, see Scheme 1. There are fully synthetic routes to generate IPN,[25] but the enzymatic

reaction is still used in large-scale production of antibiotics.[26] A detailed understanding of the enzyme-substrate interactions can help to design biosynthetic routes for β-lactam antibiotics of clinical importance.

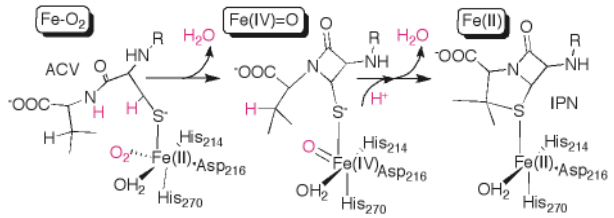

Scheme 1. General reaction scheme for isopenicillin N synthase including the proposed [Fe(IV)=O] intermediate. R=L-α-amino-δ-adipoyl.

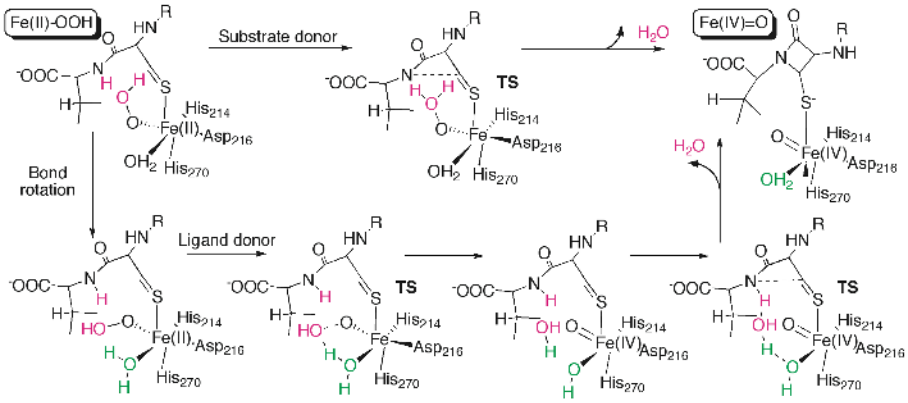

Scheme 2. Ligand donor and substrate donor mechanisms for heterolytic O–O bond cleavage and β-lactam formation.

Isopenicillin N synthase is a suitable target for QM/MM investigations because X-ray structures have been collected at different stages of the reaction, including the IPN product and an analogue of the β-lactam intermediate.[20,27] Independent deuterium kinetic isotope effects for both the cysteine β-carbon and the valine β-carbon suggests that both C–H bond activation steps are at least partially rate-limiting,[28] which gives two steps where the calculated barrier can be compared to experiment.

2. Computational Details

Methods. In a two-layer ONIOM calculation[5-8] the system is divided into two parts, a selected model system treated by a high-level (QM) method and the remainder treated by a low-level method, often molecular mechanics (MM). In this study the high-level method was the density functional B3LYP,[29,30] and the low-level method was the Amber96 force field.[31] The applicability of the ONIOM (B3LYP:Amber) method has previously been illustrated for several enzymatic systems.[32-36] Geometries were optimized at the 6-31G(d) level and final energies were evaluated with the 6-311+G(d,p) basis set.[9] Differences between active-site and ONIOM models come from the potential energy, but also from the dielectric continuum that was used to approximate the protein in the active-site model, but that was not included in the ONIOM models. Zero-point and thermal corrections were assumed to be similar between the two approaches and were taken from fully optimized active-site models.

Calculations have been performed using a private development version of Gaussian[37] that includes the "fully coupled macro/micro–iterative" optimization scheme described previously. The algorithm was initially implemented for the mechanical embedding (ME) scheme, and all optimizations have been performed with ONIOM-ME. Stationary points, including transition states, are fully optimized using the default convergence criteria, while transition state ^{5}**7S** has all but the maximum displacement converged (details in the Supporting information). Transition states are characterized by a single negative eigenvalue in the Hessian matrix.

In mechanical embedding, the electrostatic interactions between the reactive region and the surrounding protein are calculated classically. In the standard implementation the point charges assigned to the reactive region are not automatically updated. The present models use charges from ESP (Merz-Kollman) calculations. Charges are calculated for the first stationary point of each model, and the same charges are then used in all optimizations with that model. Details are given in the description of the model setup below. Standard ONIOM-ME only includes electrostatic effects due to geometrical changes but neglect the changes in the electronic structure of the model system, e.g., on charge transfer. A common alternative approach is to calculate the electrostatic interactions semi-classically, i.e., to incorporate the MM charges into the QM Hamiltonian (electronic embedding or EE).[8,38] The main advantage is that QM/MM-EE includes the exact electrostatic interaction between the electron density and the point charges in

the protein environment. In addition, QM/MM-EE self-consistently updates the response of the electron density to the external charges. However, QM/MM methods typically neglect electronic polarization of the MM part, which should lead to an overestimation of the effect of the MM charges. Optimization schemes also underestimate effects of geometric polarization as the geometry stays in the same local minima.

If a dielectric constant of four, as commonly used in protein modeling, is introduced into the Coulomb expression for electrostatic interactions, these effects decreases to ¼. ONIOM-EE should correctly indicate the presence and the direction of protein electrostatic effects, but the effects are likely to be overestimated, especially for distant residues. ONIOM-ME neglects some effects while it may overestimate others and only gives the correct energy if the total effect is small, or if there is a favorable cancellation of errors. In this report results are given at the ONIOM-ME level, because this is the level where all structures have been optimized. Reaction steps where ONIOM-EE (still using ONIOM-ME geometries) gives a significantly different description of the relative energy are discussed separately in the text.

Models. The original design of the ONIOM system was made to facilitate a comparison between previously published active-site (B3LYP) and QM:MM (B3LYP:Amber) approaches. In the first series of ONIOM models (A–C), the model system is identical to the corresponding active-site model.[9] Initially the model system includes Fe, a water ligand, selected parts of the three amino acids His214, Asp216, His270 (*Aspergillus nidulans* numbering), and the substrate (model A), see Figure 1. Model A contains 65 atoms including the link hydrogens. In the active-site study, the water formed after O–O bond cleavage was removed from the model because its mobility led to problems with artificial hydrogen bonds. In the ONIOM setup the same water was moved to the MM part in model B. For similar reasons the substrate carboxylate was moved to the MM part after β-lactam ring formation (model C). The changes in ONIOM setup were made to enable a direct comparison between the QM contribution in the active-site and the ONIOM models, and would not have been required in regular ONIOM modeling. Model A is applied to stationary points 1-9 and uses QM charges calculated at point 1. Models B (points 9-13) and C (points 13-18) use charges from stationary points 9 and 13 respectively.

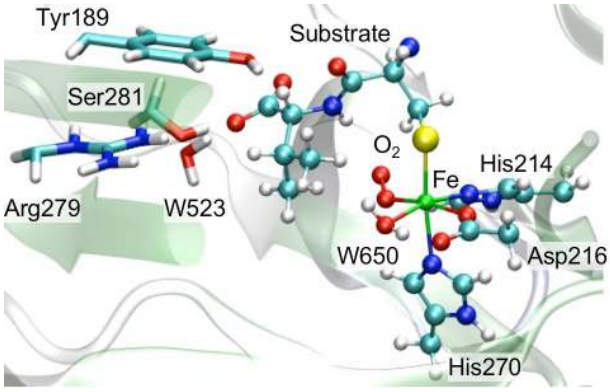

Figure 1. ONIOM QM:MM models A and D. The high-level part of model A includes all atoms in ball-and-stick representation while the high-level part of model D additionally includes residues in stick representation. Water molecules are numbered according to the PDB structure 1BLZ.

In ONIOM model D, an extension of the QM part is made by including selected parts of the side-chains of Tyr189, Arg279, Ser281, and a water molecule interacting with the substrate carboxylate, see Figure 1. The extension is made in order to improve the description of the substrate donor mechanism. The QM part of model D contains 103 atoms. The QM charges are taken from the parameterization of model A, and Amber charges are used for the newly added residues. The procedure facilitates the comparisons between model D and model A.

The setup of the real system of models A–D largely follows the procedure used to study O_2-binding in IPNS.[39] A detailed description is available in the Supporting information. The real system includes all protein atoms in the X-ray structure and crystallographic water within 20 Å from iron. No solvent water molecules were included, similar to a previous QM/MM study of camphor hydroxylation in which no major effect of solvent water could be observed.[40] The real system includes 5368 atoms, including hydrogens.

Investigations of the reaction mechanism were made with a protein structure obtained by optimization of the X-ray structure. During optimization of large systems, structural changes may occur that are not directly related to the reaction coordinate. To approximately handle these artificial changes, iterations between reactant and product states were performed until both had the same conformation of the protein environment. Transition states are also relaxed both in the forward and backward direction. This does not prove that there is a connection between reactant,

transition state and product, but at least it gives an indication about the shape of the potential energy surface. The improved ONIOM optimization algorithm minimizes the number of bad steps and helps the MM part to stay in the same local minimum during the reaction.[11]

The static optimization procedure does not take into consideration the possibility of changes in the protein configuration or large movement of water molecules. In the ligand donor mechanism, one of the reaction steps involves a proton transfer from the substrate to an iron ligand through a bridging water molecule. In the structure obtained by a static QM:MM optimization, this reaction is highly unfavorable because there is no water molecule bridging the donor and acceptor sites. To probe the possibility of other more favorable water configurations, an alternative model setup, based on a classical molecular dynamics simulation, was used for the proton transfer step in the ligand donor mechanism (model E).

Here an ensemble of starting geometries was obtained from an MD simulation with the geometry of the QM part frozen (details of the simulations are provided in the Supporting information). Calculations were performed using the program NAMD2.[41] After 2.5 ns of equilibration, a snapshot was obtained each 50 ps for 500 ps, with one additional structure selected after visual inspection of the trajectory. This gave a total of 12 different starting structures with different alignment of water molecules around the active site. Model E uses the same high-level part as model B, but the real system includes all protein atoms and all water molecules with at least one atom within 15 Å from any high-level atom. Atoms more than 12 Å from any high-level atom were kept frozen to eliminate movement at the model surface.

Additional models have been used to analyze specific reaction steps, but they only include minor modifications and will therefore be introduced in the Results section.

3. Results

The effects of the protein will be described by following the reaction from the iron-bound dioxygen species until the formation of the thiazolidine ring. The term “protein effect” is used for changes in relative energy when going from the active-site model (without explicit treatment of the protein matrix) to the QM:MM protein model. It is not a stringent definition because it

depends on the choice of model system. In the present comparison, the active-site model only includes a minimum amount of residues, and this should give large protein effects.

Whether the protein effect is considered significant depends on the properties of interest. If the purpose is to propose a general reaction mechanism, a protein effect of a few kcal/mol does not change the conclusions because the high-level hybrid DFT method has an error of ~5 kcal/mol,[42] and the window for accepting mechanisms based on the barrier height is therefore rather wide. However, when discussing rates of competing reactions, a protein effect of 3 kcal/mol can determine the relative product distribution.

The biosynthesis of isopenicillin N involves a large number of stationary points, and to facilitate the discussion each point is assigned a number (appearing in bold face) according to the order in which it appears along the reaction coordinate. The nature of the stationary point is indicated with TS for a transition state and INT for reaction intermediate. A left superscript shows the spin multiplicity of the state. For example, the label ^{5}**3** TS is assigned to the third stationary point on the quintet spin surface, which is a transition state. Transition states have not been optimized for some minor steps, e.g., bond rotation, and two intermediates may therefore appear next to each other in the reaction energy diagram.

3.1. Transition state for Cys-β-C–H bond activation.

The reaction is initiated by binding of dioxygen to the metal center. Our previous ONIOM QM:MM study showed that explicit inclusion of the protein stabilized the O_2-bound state by 8–10 kcal/mol by improving the description of the metal coordination geometry and the van der Waals interactions.[39] In the ONIOM model, binding of dioxygen was close to thermoneutral (+1.0 for O_2 bound end-on and +2.5 kcal/mol for side-on binding). For completeness, the initial [Fe(II) + O_2] state is included in the energy diagram, but to be consistent with reference 9, the structure with O_2 bound side-on (^{7}**1** Reactant) is taken as the zero-energy level in the energy diagram below.

Oxygen binding gives a ferric superoxide where an electron from iron has been transferred to an antibonding π*-orbital on oxygen. Spectroscopic studies highlight the role of charge donation from the ACV thiolate ligand that renders the formation of the ferric superoxo complex energetically more favorable.[22] The six unpaired electrons required to form the septet come from the parallel alignment of the unpaired spin on the superoxide with the spins from the

five d-electrons of Fe(III). As the quintet state is the most reactive in C–H bond activation,[9] the unpaired electron on the superoxo must first flip, but this spin transition does not affect the rate of the reaction.[43] In the quintet spin state, the end-on structure (^{5}**2** INT) is the most stable, and this structure is in good alignment to abstract hydrogen from the Cys β-carbon.[22] Compared to the active-site model, explicit inclusion of the protein mainly affects the position of the hydrophobic side chain of the valine and the orientation of the amino acid ligands, but has only small effects on the alignment of the reactive superoxide or the cysteine part of the substrate, see Figure 2.

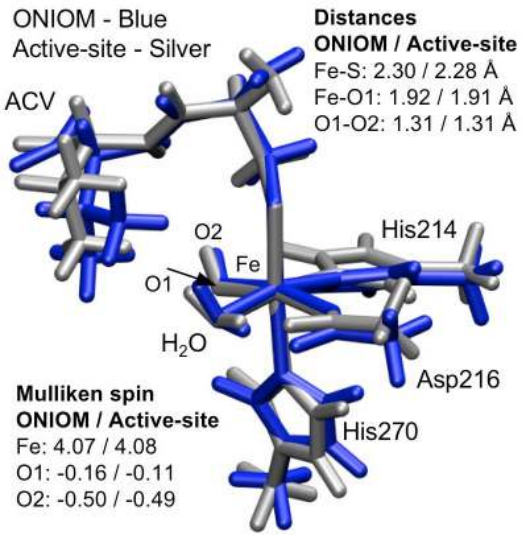

Figure 2. Geometries and spin populations for the intermediate with end-on bound dioxygen in the quintet state (^{5}**2** INT) optimized using the active-site model (silver) and the ONIOM QM:MM model (blue).

After probing the reaction coordinate using the C1–H1 and the O2–H1 distances, (see Figure 3 for labels) a transition state for C–H bond activation (^{5}**3** TS) could be fully optimized in the "fully coupled macro/micro–iterative" optimization scheme. The same method, i.e., initial mapping of the reactive space using one or two reaction coordinates followed by full optimization, has been used for all transition states.

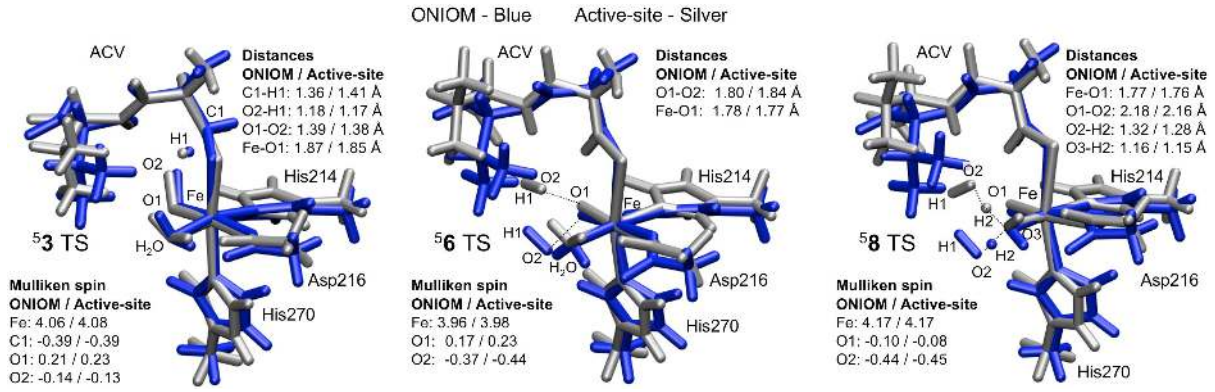

Figure 3. Geometries and spin populations of the transition states for; Cys-β-C–H bond activation ^{5}**3** TS (left), initial O–O bond cleavage in the ligand donor mechanism ^{5}**6** TS (middle), and water formation ^{5}**8** TS. The active-site model is shown in silver and the high-level part of the ONIOM QM:MM model is shown in blue.

Compared to the end-on quintet state (^{5}**2** INT), the relative energy of the transition state ^{5}**3** is 10.2 kcal/mol in the ONIOM model compared to 11.7 kcal/mol in the active-site model, see Figure 4. Using ONIOM-EE instead of ONIOM-ME has a limited effect (+0.2 kcal/mol). The relatively small effect of the protein environment on the C–H bond activation step can be rationalized from the nature of the reaction. The Mulliken spin populations, see Figure 3, show significant spin (-0.39) building up on the Cys β-carbon, indicative of a hydrogen atom transfer for which no large electrostatic effects should be expected. Further, the reaction does not require any major geometrical changes, and potential steric effects of protein are limited. The structural differences in the alignment of the valine side chain and the histidine ligands are seen already in the reactant structure (compare Figure 2 and Figure 3) and should not affect the relative energy between ^{5}**2** INT and ^{5}**3** TS.

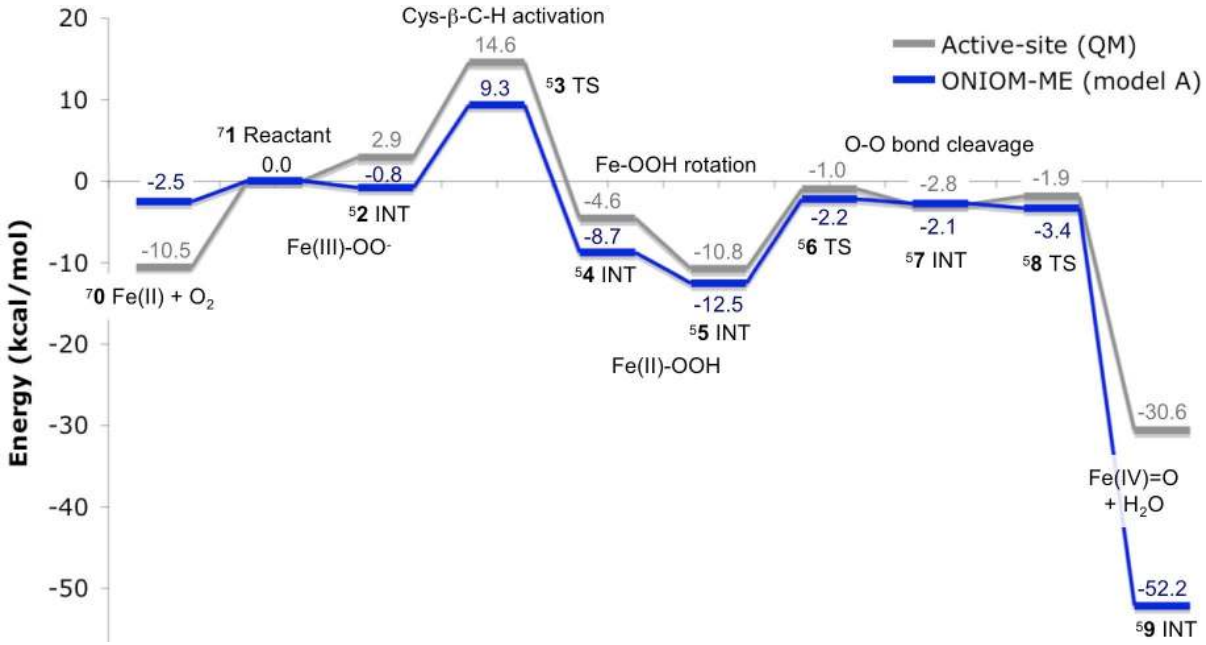

Figure 4. Energy diagrams for formation of [Fe(IV)=oxo] in the ligand donor mechanism. Energies calculated with the active-site model are shown in grey while energies from the ONIOM-ME QM:MM system are shown in blue.

Based on these considerations, the origin of the 1.5-kcal/mol effect is not easy to pinpoint. The most significant geometric effect is a decrease in the C–H bond distance from 1.41 Å in the active-site structure to 1.36 Å with QM:MM, leading to a shorter donor-acceptor distance that may facilitate the reaction. In summary, the barrier of the C–H bond activation step from ^{5}**2** INT to ^{5}**3** TS is mainly determined by the electronic properties of the iron center with only minor effects of the surrounding protein.

However, the total reaction barrier must be calculated from the lowest preceding intermediate, which in both models still is the state before oxygen binding, see Figure 4. As the QM:MM model stabilizes the end-on quintet state by >10 kcal/mol, the total C–H bond activation barrier in the QM:MM model is only 11.8 kcal/mol. This step is proposed to be partially rate limiting and the barrier, as calculated by transition state theory, should be close to 16.8 kcal/mol.[44] The modeled reaction barrier is thus underestimated by 5 kcal/mol.

After passing the transition state, the system reaches a ferrous peroxide [Fe(II)–OOH] intermediate (^{5}**4** INT). Formation of this product requires that one proton and *two* electrons are transferred from the substrate. This does not contradict the observation that the transition state

describes hydrogen atom transfer, because intrinsic reaction coordinate (IRC) calculations showed that the second electron is transferred only after passing the transition state.[9] The relative energy of the ferrous peroxide intermediate is similar in active-site and ONIOM-ME models when the preceding intermediate ^{5}**2** is used as reference, see Figure 4. However, the protein effect of the "electron transfer" from substrate to iron that occurs after ^{5}**3** TS is not properly included in any of these models. The effect on the relative energy of ^{5}**4** INT of applying ONIOM-EE instead of ONIOM-ME is large, approx. +8 kcal/mol, even after geometry relaxation at the ONIOM-EE level.

3.2. Transition states for O–O bond cleavage – ligand donor mechanism.

The next step in the reaction is closing of the β-lactam ring together with formation of [Fe(IV)=oxo]. In the active-site study,[9] a new mechanism for O–O bond cleavage was proposed in which the water ligand acts as a proton donor. The first step in this mechanism is rotation of the peroxide (^{5}**4** → ^{5}**5**) to align the outer oxygen in a position where it can accept a proton from the water ligand. This bond rotation is slightly less exothermal (by 2.4 kcal/mol) than in the active-site model, because the QM:MM model includes the original protein-carboxylate interactions at the MM level, which prevents formation of artificial hydrogen bonds between peroxide and substrate carboxylate, see Figure 5. The same effect was seen in a larger active-site model that included residues interacting with the carboxylate (Tyr189, Arg279 and Ser281),[9] but if the purpose is simply to keep the hydrogen bond network intact a QM:MM model is significantly cheaper than a large QM model. The reason the energetic effect is still relatively small is that a large part of the error in the active-site model disappears when the solvent correction is included.

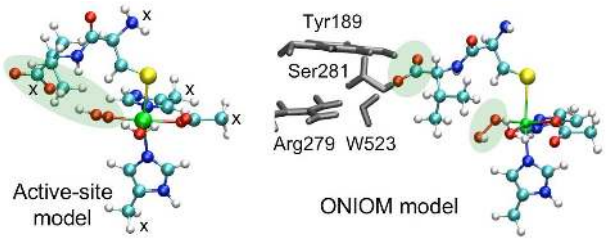

Figure 5. The QM:MM model (right) avoids artificial hydrogen bonds between peroxide and the valine carboxylate group in the Fe(II)-OOH intermediate ^{5}**5**. The active-site model (left) is optimized with atoms frozen in the position from the X-ray structure (marked with X). The QM:MM model has the same size of the QM region, but include MM residues hydrogen bonding to the carboxylate in the QM:MM description (shown in grey), as well as all other protein residues.

O–O bond cleavage in the ligand donor mechanism proceeds by initial electron transfer from iron to an antibonding O–O σ* orbital (^{5}**6** TS). This process leads to a shallow minimum with a long O–O bond (^{5}**7** INT) that quickly abstracts a proton from the water ligand and a second electron from iron to form water, see reference 9 for details. O–O bond cleavage is similarly described in the active-site and the ONIOM models, but the orientation of the donating water and the peroxide changes due to the difference in the initial position of the peroxide, see Figure 3. The effect on the relative energies is small with the barrier for ^{5}**6** TS going from 9.8 kcal/mol in the active-site model to 10.3 kcal/mol in the ONIOM model, see Figure 4. The second transition state (^{5}**8** TS) disappears after adding corrections for thermal effects and large basis, but whether the intermediate ^{5}**7** appears on the calculated potential energy surface seems to be determined by minor details, and for all practical purposes, O–O bond heterolysis can be considered as a concerted reaction.

The first step, from ^{5}**5** INT to ^{5}**6** TS**,** is an electron transfer from iron to oxygen and there is a non-negligible effect when going to ONIOM-EE (+5.9 kcal/mol at the ONIOM-ME geometry). Such a large effect would make this step potentially rate limiting, but as argued before, it is likely to be overestimated.

The total O–O bond cleavage reaction is heterolytic and leads to formation of a water molecule and an [HO–Fe(IV)=O] intermediate (^{5}**9**). Unlike the previous reaction steps, the protein effect is very large, -20.1 kcal/mol, see Figure 4. The effect comes from interactions

between the released water and atoms outside the QM model. In the active-site model the newly formed water bridged the valine N–H group and the iron hydroxo ligand. In the ONIOM model the same water makes hydrogen bonds with explicit MM waters instead of the substrate, see Figure 6, which leads to large effects on the reaction energy for this step. As a general observation, release of a product shows large protein effects due to explicit interactions with residues not included in the active-site model. These effects are also sensitive to the choice of mechanical or electronic embedding.

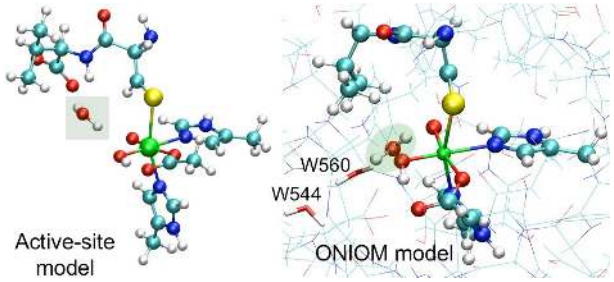

Figure 6. Different alignment of the water formed after O–O bond heterolysis, highlighted in green, in active-site and ONIOM models. Selected water residues in the MM description are shown in stick representation.

3.3. Transition state for β-lactam ring formation – ligand donor mechanism.

To conclude the formation of the β-lactam ring, the valine N–H proton should be transferred to the hydroxyl ligand at the same time as the C–N bond of the four-membered β-lactam ring is formed, see Scheme 2. However, the barrier for the first step in this mechanism (^{5}**10** TS) becomes unreasonably high (>45 kcal/mol) in the original ONIOM model. The corresponding barrier was ~11 kcal/mol in the active-site model, so the protein effect is >30 kcal/mol. The large effect is different from what was observed for C–H bond activation (^{5}**3** TS) and O–O bond cleavage (^{5}**6** and ^{5}**8** TS), but similar to the effect on the preceding water formation step. The reason is that to function as a proton relay in ^{5}**10** TS the QM water must return to the position where it bridges the valine N–H group and the hydroxo ligand. The QM:MM interactions that stabilized water release are lost in the transition state, which leads to an exceedingly high barrier.

A deficiency in the optimization approach is the relatively static description of the protein that usually leads to small changes in the position of different groups. This is problematic when

handling potentially mobile water molecules. In the ligand donor mechanism, the barrier for β-lactam ring formation is sensitive to the position of a single water molecule, exactly the kind of situation that the optimization approach has problems to handle. It is possible that the required bridging position is empty because water molecules inside the protein simply cannot move to the desired position during an optimization.

To find configurations where water is bridging the substrate and the iron ligand, twelve snapshots were taken from a molecular dynamics (MD) equilibration with the QM coordinates frozen from ^{5}**10** TS as described in the Computational details (model E).Proton transfer barriers were calculated by separately optimizing the reactant and a transition state guess with frozen proton-transfer coordinates from the MD snapshot.

This approach gave barriers ranging from 20.8 to 43.3 kcal/mol, and the major difference comes from the low-level MM contribution, see Figure 7. The large variability in the barrier height reflects the number of conformations available for water molecules around the active site, see Figure S1. Taking the lowest barrier (snapshot at 2.75 ns) and performing a full transition state optimization of the QM:MM model gives a barrier of 20.7 kcal/mol. As an alternative, taking the structure with the highest barrier for a single water bridge (2.54 ns snapshot) and transferring the proton using one additional QM water (model F) leads to an optimized barrier of 21.0 kcal/mol, see Figure S2.

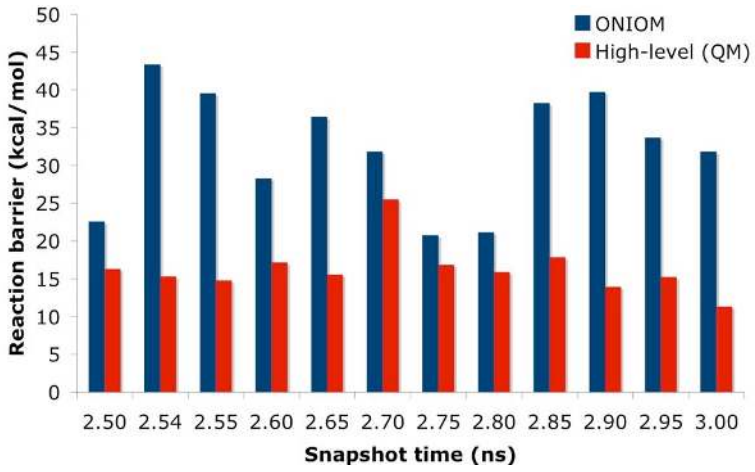

Figure 7. Proton transfer barriers (^{5}**10** TS) for different snapshots from a molecular dynamics trajectory. In the snapshot at 2.7 ps, the QM barrier is high because the accepting hydroxo ligand has lost its hydrogen bond to Asp216.

The calculated barrier of ~21 kcal/mol is high compared to the experimental limit of 17 kcal/mol, despite the fact that performing the MD simulation with the QM geometry frozen at the transition state could overestimate the stability of that state and underestimate the barrier height. However, the modeled reaction is restricted to residues in the QM system and alternative pathways may be available in the real protein. The ligand donor mechanism can therefore not be excluded. Instead, the most important conclusion is that barriers for reactions involving mobile water molecules cannot be consistently modeled with pure optimization schemes.

3.4. Transition states for O–O bond cleavage and β-lactam formation - substrate donor mechanism.

The most direct way to close the β-lactam ring is to use the valine N–H proton during O–O bond cleavage, see Scheme 2. Previous active-site investigations[9,24] could not find a low-energy path for the substrate donor mechanism. With ONIOM model A the search for the substrate donor pathway eventually led to the electron transfer required to weaken the O–O bond, but the electron came from the substrate carboxylate, not from iron. The observed reaction was therefore decarboxylation rather than β-lactam formation. From this observation it is clear that the problem with model A (in active-site and ONIOM-ME) is that the ionization potential of the carboxylate is underestimated unless its hydrogen-bonding residues are included. To handle this deficiency, the QM system is extended by including residues closest to the valine carboxylate (Tyr189, Arg279, Ser281, and W523), see model D in Figure 1. The same extension of the active-site model in reference 9 would also have been sufficient. This illustrates the importance of including a large QM part in active-site and QM:MM-ME calculations. The advantage of the QM:MM model is that it allows the additional QM residues to move with the substrate without the risk of creating new artificial hydrogen bonds.

Starting from the [Fe(II)-OOH] intermediate ^{5}**4**, see Figure 8, the reaction proceeds through three separate transition states, although no long-lived intermediate is expected to appear along the pathway. The initial reaction coordinate is elongation of the O–O bond, coupled to electron transfer from iron. Passing ^{5}**5S** TS at an O–O bond distance of 1.73 Å, see Figure 9, has a barrier of 7.8 kcal/mol and leads to an intermediate with a long (2.17 Å) O–O bond (^{5}**6S** INT). The additional label **S** refers to intermediates appearing only along the substrate donor pathway.

Further O–O bond elongation leads to a second electron transfer from iron to the leaving hydroxyl and the valine N–H proton is transferred from the substrate to complete the formation of water (^{5}**7S** TS). This leads to a high-energy ferryl-oxo structure (^{5}**8S** INT) with a linear substrate that quickly undergoes cyclization (^{5}**9S** TS) to form the β-lactam ring (^{5}**10S** INT). All transition states along the pathway are shown in Figure 9. The highest barrier, 9.3 kcal/mol, is observed for proton transfer from the substrate (^{5}**7S** TS), while cyclization, i.e., C–N bond formation (^{5}**9S** TS), has a barrier of only 2.8 kcal/mol compared to the peroxide intermediate ^{5}**4** INT, see Figure 10.

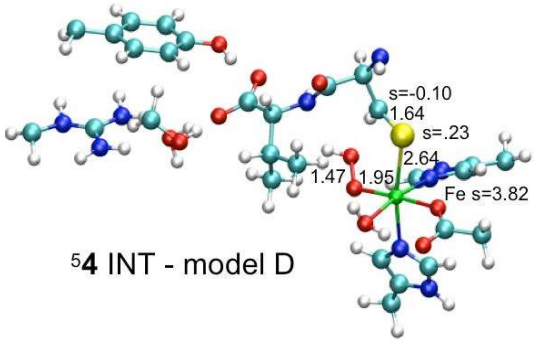

Figure 8. Geometry and spin population of the [Fe(II)-OOH] intermediate ^{5}**4** optimized with ONIOM model D.

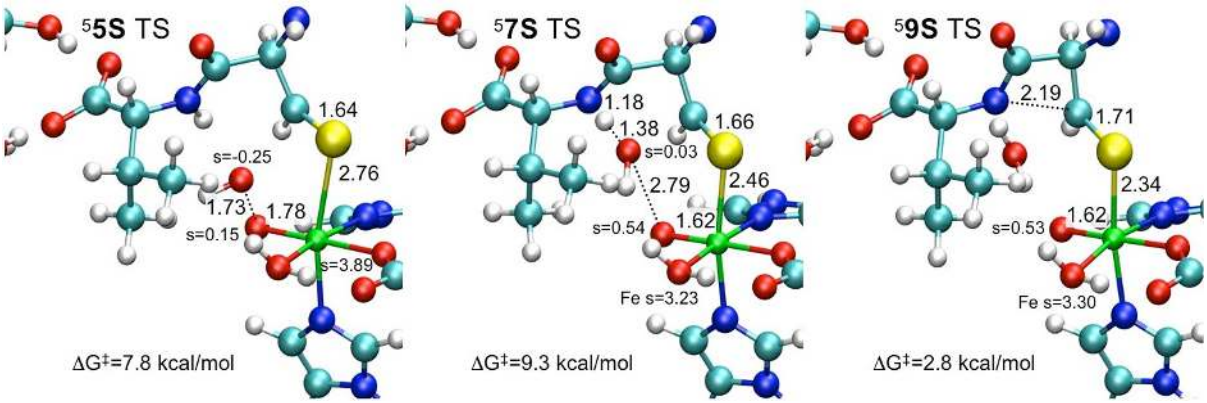

Figure 9. Close-ups of the transition states for heterolytic O-O bond cleavage and β-lactam formation in the "substrate donor" mechanism. Labels show important bond distances in Å and Mulliken spin populations.

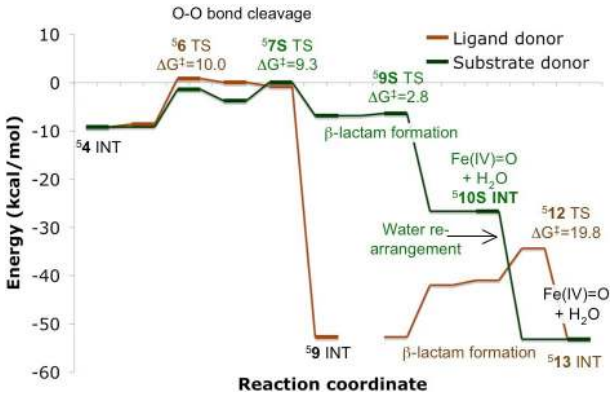

Figure 10. Energy diagram for formation of the β-lactam + [Fe(IV)=oxo] intermediate from [Fe(II)-OOH] in substrate and ligand donor mechanisms using model D. The energies for β-lactam ring closure in the ligand donor mechanism (thin brown line) are taken from the active-site model.

After formation of water and the β-lactam ring, the relative energy of ^{5}**10S** INT is much higher than the energy of the corresponding [Fe(IV)=oxo] intermediate ^{5}**13** INT along the ligand donor pathway. In ^{5}**10S** the water formed during O–O bond heterolysis remains in the hydrophobic pocket trans to Asp216, but it is assumed that it can rearrange to reach the low-energy structure observed in the ligand donor pathway.

To be able to directly compare the ligand and substrate donor mechanisms, the former mechanism was reoptimized using model D, see Figure 10. Compared to model A with its smaller model system, the changes in transition state barriers are relatively small (-0.3 kcal/mol for ^{5}**6** TS and -0.6 kcal/mol for ^{5}**8** TS).

The barrier for O–O bond cleavage in the substrate donor mechanism, 9.3 kcal/mol, is slightly lower than the highest barrier in the ligand donor mechanism, 10.0 kcal/mol, see Figure 10. Single point calculations using ONIOM-EE gives a much larger difference in barrier height (8.5 kcal/mol), mainly due to the electrostatic effects on O–O bond cleavage in the ligand donor mechanism. Even if the effect is overestimated, it is still likely that electrostatic interactions favor the substrate donor pathway by a few kcal/mol.

3.5. Transition state for Val-β-C–H bond activation.

After formation of the [Fe(IV)=oxo] intermediate, the reaction proceeds by C–H bond activation at the valine β-carbon. Using the optimized structure obtained from previous modeling (^{5}**13** INT), the valine side chain must rotate almost 180° to align the C–H bond towards the iron center (^{5}**14** INT). This is a difficult reaction to model, because it could be accompanied by changes in the conformation of the hydrophobic residues surrounding the side chain. In ONIOM model C, which is similar to model A, the rotation leads to movement of the newly formed water, but the reaction energy for bond rotation is the same in the active-site and ONIOM models (+0.9 kcal/mol).

Activation of the Val-β-C–H bond (^{5}**15** TS) is a hydrogen atom transfer, and the effect of the protein is expected to be small, as it was for the activation of the corresponding Cys-β-C–H bond. On the contrary, in ONIOM model C the reaction barrier becomes 22.0 kcal/mol compared to 15.3 kcal/mol in the active-site model, see Figure 11. This is a significant effect, but it makes the barrier much higher than the experimental value of ~17 kcal/mol for this partly rate-limiting step.

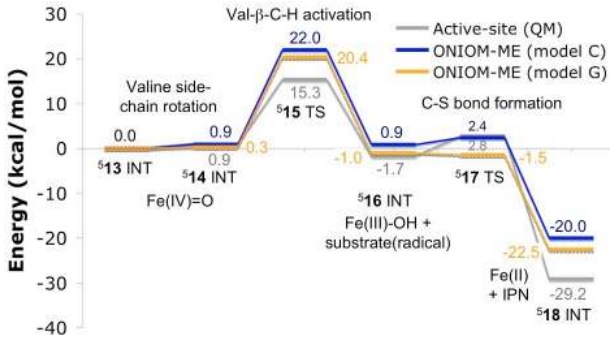

Figure 11. Energy diagrams for Val-β-C–H bond activation and thiazolidine ring closure with the active-site model and ONIOM models C and G. Values of relative energies are placed below the line for the active-site model, above the line for ONIOM model C and on the side for ONIOM model G.

What distinguishes this reaction from the previous C–H bond activation (^{5}**3** TS) is that it requires a large movement of the substrate, because the valine side chain must approach the oxo group. All comparisons of the optimized structures from active-site and ONIOM models show

large differences in the alignment of the valine side-chain, see e.g., Figure 2. This is true also in the transition state ^{5}**15** TS, although the effect on the reaction coordinate is less obvious. The ONIOM model has a longer C2-H3 distance and a slightly shorter O1-H3 distance, see Figure 12.

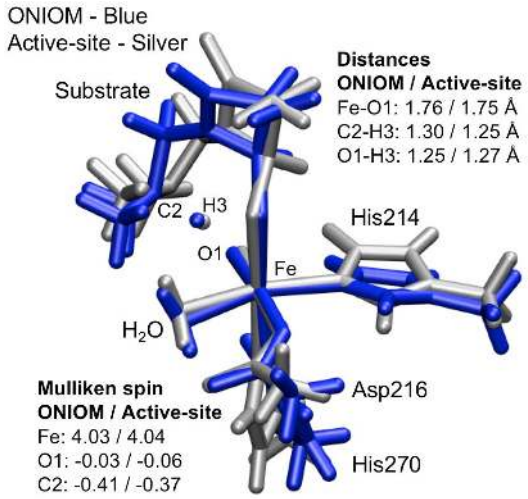

Figure 12. Geometries and spin populations for the transition state for Valine-β-C–H bond activation (^{5}**15** TS) optimized using the active-site model (silver) and the ONIOM QM:MM model C (blue).

In the active-site model the transition state was favored by 3.5 kcal/mol by the IEFPCM solvent description because the movement of the side chain leads to a more compact QM region and therefore a decrease in the cavitation energy. Explicit inclusion of the protein in model C instead disfavors the transition state by 3.2 kcal/mol (+2.9 at the high level and +0.3 kcal/mol from the low level). The sum of these two effects leads to the large difference between the ONIOM and the active-site model.

As the barrier in the ONIOM model is too high compared to experiment, several attempts were made to find a lower barrier. Applying model D with its larger QM part did not change the total barrier from ^{5}**13** INT, and the barrier was not stabilized with ONIOM-EE (effect of +0.8 kcal/mol). The reaction pathway was also optimized on the septet and the triplet surfaces, but the barriers were higher in energy (by 3.6 kcal/mol for ^{7}**15** TS and by 3.7 kcal/mol for ^{3}**15** TS).

In order to check for major errors in the structure, the optimized structure of ^{5}**13** INT was compared with an X-ray structure of ACmC, that forms an analogue of the monocyclic β-lactam intermediate.[27] The major structural differences are in the arrangement of the water molecules. In the ONIOM structure the newly formed water molecule is located close to the oxo ligand trans to Asp216, but there is no water in that position in the X-ray structure of the ACmC substrate. Furthermore, there is no water in the corresponding pocket in the X-ray structure with ACV and NO[20] or in the structure of the IPN product, see Figures S3 and S4.[27] The presence of a water molecule in that position was investigated by classical MD simulations. In these simulations, the QM region was kept frozen (except the water molecule and the hydrophobic valine side chain). After a few picoseconds water leaves its position close to the oxo group and does not return. Details of the MD simulations are given in the supporting information.

Consequently, it was assumed that the water molecule leaves the active site through the channel occupied by WAT544 and WAT560 in the X-ray structure, see Figure 6. This process is difficult to model, and the water molecule was simply removed from model D to form the new ONIOM model G. Optimization of the C–H activation transition state with the new model gave a total barrier of 20.4 kcal/mol, 1.6 kcal/mol lower than models with a water in close to the oxo group, see Figure 11.

The product of the C–H bond activation is a ferric hydroxo species and a substrate radical located on the valine-β-carbon (^{7}**16** INT). The relative energy of this intermediate is rather similar in all different models.

3.6. Transition state for thiazolidine ring formation.

From the substrate radical state (^{5}**16** INT) the five-membered thiazolidine ring can be formed by an attack of the carbon radical on sulfur. Compared to the QM model, the ONIOM transition state for C–S bond formation (^{5}**17** TS) does not change much (from 2.73 Å in the active-site model to by 2.71 Å), but the barrier drops from 4.5 kcal/mol to 1.5 kcal/mol compared to the preceding intermediate ^{5}**16** INT. A tentative explanation for the decrease in barrier is that the protein favorably aligns the valine β-carbon radical for a reaction with the thiolate, see Figure 13. A geometric indication is that the C–S distance in the reactant is 3.6 Å in the protein and slightly longer in the active-site structure (3.79 Å). The barrier height is sensitive to the choice of

QM model because in both models with larger QM part (D and G), the barrier disappears after the basis set correction has been applied, see Figure 11.

Formation of the thiazolidine ring includes a final electron transfer from the thiolate to iron to regenerate Fe(II), and again there is a significant difference between ONIOM-ME and ONIOM-EE (+3–4 kcal/mol at the ONIOM-ME geometry for different models).

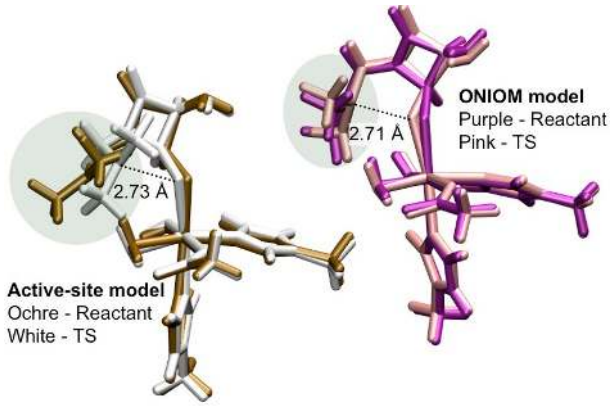

Figure 13. Reactant and transition state for thiazolidine ring formation in the active-site model (left) and ONIOM model C (right). The improved alignment of the substrate side chain in the ONIOM model is highlighted in blue.

Formation of the C–S bond creates the thiazolidine ring and completes the formation of the bicyclic IPN product (^{5}**18** INT). The reaction decreases the strength of the substrate-metal coordination, and in all models the substrate loses its coordination to iron. The energy of product formation is rather different in the active-site and the ONIOM models, see Figure 11. The ONIOM models give much shorter Fe–S bond distances (3.2-3.5 Å) compared to the active-site model (Fe–S distance of 4.2 Å).

However, the Fe–S distance is still much longer than in the X-ray structure of the IPN product (Fe–S distance of 2.87 Å, see Figure S3). In the X-ray structure, the water formed during the second part of the reaction has already left the active site and iron is five-coordinated.[27] This is different from the final optimized structure ^{5}**18** INT that still has a hydroxyl ligand trans to Asp216. To complete the enzymatic reaction the hydroxyl group should receive a proton and form water. This proton is equivalent to the proton lost from the thiol during the initial binding of ACV, but these processes are not modeled because no proton acceptor/donor was included in the

QM part. Attempts to reproduce the Fe–S distance in the product X-ray structure using a model with a water ligand (model H) or a model with five-coordinate iron (model I) did not succeed (Fe–S distances >3.2 Å). The QM:MM models still has problems to describe structures with very weak metal ligand interactions that are balanced by large changes in the MM interactions during substrate release.

4. Discussion

4.1. Transition state effects.

The reaction barrier is the most common computational criterion when discriminating between different reaction mechanisms. In the present study, the ease in which transition states can be optimized allows for a broad comparison of protein effects on different types of transition states.

The effects of the protein in the current study are either steric or electrostatic, and can be rationalized by considering whether the transition state involves large movements of the substrate, or whether it involves electron transfer. In the ONIOM-ME description, the protein effect is small (~1–2 kcal/mol) for transition states; ^{5}**3** (Cys-β-C–H bond activation), ^{5}**6**, and ^{5}**8** (O–O bond cleavage) because they lead to relatively small changes in the active site structure, see Figure 3. Although not compared to an active-site model, transition states ^{5}**5S** and ^{5}**7S** (O–O bond cleavage) in Figure 9 also belong to this category. Protein effects are larger (3–6 kcal/mol) for transition states that involve movement of the hydrophobic side chain, i.e., ^{5}**15** (Val-β-C–H bond activation) and ^{5}**17** (thiazolidine ring formation), see Figures 12 and 13. The transition state for β-lactam ring closure, ^{5}**9S** in Figure 9, is likely to belong to this category. The absolutely largest protein effect is observed for the transition state ^{5}**10** (proton transfer) that requires rearrangement of a mobile water molecule, a situation that is not handled well with the present approach.

In the single-point ONIOM-EE description, electrostatic effects become significant (>4 kcal/mol) for the transition states ^{5}**6** (O–O bond cleavage) and ^{5}**17** (thiazolidine ring formation) that include electron transfer between substrate and iron. In both cases the effect leads to an increase in the barrier. The transition states for O–O bond cleavage in the substrate donor mechanism (^{5}**5S** and ^{5}**7S**) also involve electron transfer, but the effects of applying ONIOM-EE

are small. A rough rationalization of the electrostatic effects can be made by considering the "direction" of electron transfer relative to the electric field of the protein, see Figure 14. The electrostatic interactions favor the substrate donor pathway because the critical electron transfer from iron to the anti-bonding O–O π* orbital proceeds perpendicular to the electric field, while in the ligand donor mechanism it proceeds partly in the direction of the electric field. Although the electrostatic effects are difficult to calculate correctly, control of the reactivity in IPNS by a directional electric field is an interesting concept that requires a more careful investigation.

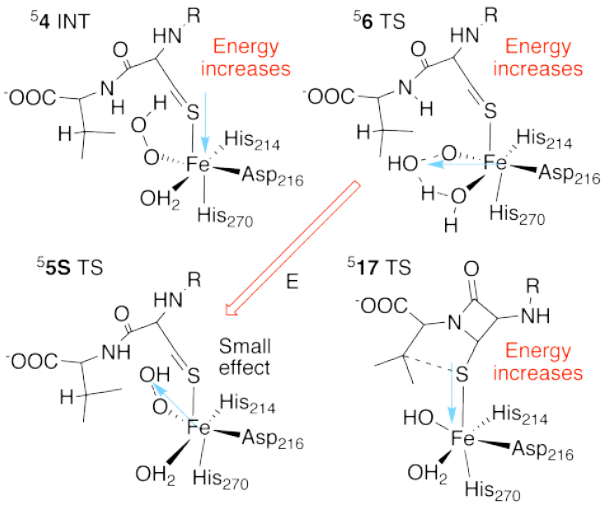

Figure 14. Cartoon to rationalize electrostatic effects on electron transfer in the ONIOM-EE description. The red arrow shows the rough direction of the electric field while blue arrows show the estimated "direction" of electron transfer.

In principle, both ligand and substrate donor routes could be active as they lead to the same [Fe(IV)=oxo] state (^{5}**13** INT), assuming that there really is a proton transfer pathway from substrate to the iron ligand W650. The difference between the two mechanisms could become clearer by studying the enzymatic reaction with the alternative ACOV substrate. The major difference between the normal substrate (ACV) and ACOV is that the latter lacks a valine N–H proton. The substrate donor mechanism is therefore not viable. Experimentally, reactions with ACOV lead to hydroxylation of the Cys-β-carbon, presumably by the iron bound peroxide (^{5}**4** INT).[45] In the ligand donor mechanism, the [Fe(IV)=oxo] species (^{5}**9** INT) can still be generated

without the substrate proton. If it can be shown that the ferryl-oxo intermediate does not lead to hydroxylation of the Cys-β-carbon, the ligand donor mechanism can be ruled out.

4.2 Other significant protein effects.

As the real transition state barrier should be calculated against the lowest preceding intermediate, relative energies of intermediates can affect the rate of a reaction step. As an example, the barrier for the first C–H bond activation step, ^{5}**3** TS in Figure 4, decreases significantly when the protein is included, mainly due to the failures of the active-site model to describe O_2 binding.[39] In the present study, large effects on relative energies are found for reactions involving formation of water and the IPN product. These effects are handled mainly at the MM level and are difficult to describe accurately. Fortunately, the effects are not critical when determining the reaction mechanisms because product formation is often exothermal and the degree of exothermicity has no effect on the barrier of the next step. As an example, the barrier for Cys-β-C–H bond activation is not affected by the calculated exothermicity of β-lactam formation.

Formation of the [Fe(II)-OOH] species (^{5}**4** INT) shows large electrostatic effects with ONIOM-EE because it involves electron transfer from substrate to iron. As long as peroxide formation is still an exothermal reaction, this should not affect the rate of O–O bond cleavage.

4.3 Modeling accuracy.

Assuming that the two C–H bond activation transition states both are partially rate-limiting with barriers of ~17 kcal/mol, the discrepancy between experiment and calculation is 5 and 3 kcal/mol, respectively. This not considered a reason to reevaluate the mechanism, because 3–5 kcal/mol is within the expected accuracy for density functional calculations of transition metal systems. The first C–H bond activation (^{5}**3** TS) is a simple hydrogen atom transfer from the substrate to the superoxo radical, a reaction type for which DFT might underestimate the barrier. The second C–H bond activation (^{5}**15** TS) is also a hydrogen atom transfer, but here the reaction barrier is overestimated. A significant difference is that this C–H bond activation requires a change in the electronic configuration of the iron-oxo bond, a situation where trends from simple organic reactions may no longer hold. A possible reason for the too high barrier for ^{5}**15** TS is that the optimization to the *closest* local minimum may not allow the protein model to relax properly. This could overestimate the energy required to move the substrate towards the oxo group.

There are also shortcomings in the description of the protein interactions. As discussed in the Computational details, mechanical embedding largely neglects protein effects on electron transfer while electronic embedding qualitatively gives a better description of the direction of the electrostatic effects, but is likely to overestimate the effects due to lack of polarization of the MM part. We are at present testing improved optimization algorithms for electronic embedding, as well as two-layer DFT:DFTB[46,47] and three-layer DFT:DFTB:MM models that naturally include electronic polarization and charge transfer effects through an inexpensive QM layer.

Another issue concerns the setup of the model, especially water molecules whose positions are not well determined, but still can have large effects in QM:MM calculations.[48,49] This is illustrated by the large differences in barrier for water-mediated proton transfer (^{5}**10** TS, see Figure 7). A related problem is the uncertainty in the position of the water molecule formed after O–O bond heterolysis. In the present static study, two alternatives have been accounted for, one where the water is located close to the oxo group, and one where it has been removed from the system. The latter choice is supported by a separate molecular dynamics simulation. It also leads to a lower barrier for C–H bond activation by ~2 kcal/mol.

4.4. Catalytic efficiency of the metal center.

The low barriers achieved with an active-site model indicated that the main catalytic effect of IPNS comes from the metal center. In principle agreement with experiment can be achieved with a method that consequently underestimates barriers together with a neglect of the "real" protein effects. A QM/MM model that includes an explicit description of the protein is therefore a better argument for the catalytic proficiency of the non-heme iron center. The competence of the metal center is also shown by the reactivity of biomimetic complexes,[17,50,51] although they do not show the same efficiency and specificity as the enzymatic reactions.

4.5. Protein control of IPNS reactivity.

Apart from the initial O_2-binding step, the suggested role of the protein in IPNS is to control the reactivity of the metal center. One example is the effect of the hydrophobic side chains that orient the valine side chain in an orientation that is favorable for thiazolidine ring formation. Although not important for the total reaction rate, this protein effect may prevent side reactions of the substrate radical. It has previously been observed that mutations of the hydrophobic

residue Leu223 lining the valine side chain leads to changes in the product ratio for an alternative substrate.[52] The conclusion was that the bulky side chain hinders the rotation of the substrate in the native enzyme. These two mechanisms may work in concert to achieve high product and stereospecificity in IPNS.[53]

An important result of the ONIOM calculations is the detailed description of the substrate donor mechanism for β-lactam formation. However, the reason this pathway could be found was not the long-range protein effects, but that the QM:MM model made it easier to include residues close to the substrate while still keeping the hydrogen bonds intact during β-lactam ring formation. The residues (Tyr189, Arg279, Ser281, and W523) can have a role in preventing side reactions, e.g., decarboxylation or cleavage of the C–C bond between the carbonyl and the carboxylate.

5. Conclusions

With the new quadratically coupled QM/MM geometry optimization algorithm it is feasible to locate transition states in protein systems, similar as in single-layer QM calculations. The optimization procedure allows for a direct evaluation of protein effects on all the transition states appearing along the reaction pathway of isopenicillin N synthase. The effects are typically smaller than 4 kcal/mol and can be understood by considering whether the transition state involves large movements of the substrate and whether it involves electron transfer.

The lack of major stabilizing protein effects on the rate-limiting transition states of IPNS suggest that a large part of the catalytic effect comes from the metal center. The suggested role of the protein is to control the reaction and achieve high product specificity. Hydrophobic residues align the valine substrate radical in a favorable conformation for thiazolidine ring closure and contribute to the product selectivity and high stereospecificity of the reaction. An interesting possibility that merits further investigation is that the mechanism for heterolytic O–O bond cleavage is determined by the direction of the electric field at the active site.

A detailed comparison of the polarization/charge transfer effects in the ONIOM QM:MM-EE, QM:QM and QM:QM:MM models will be presented in a separate paper. Another extension is to include statistical averaging of the protein effects over an ensemble of MM

configurations. Detailed studies on this aspect using free-energy perturbation and other methods will also be discussed separately.

Acknowledgement: One of the authors (ML) acknowledges a Fukui Institute for Fundamental Chemistry Fellowship. The work was in part supported by a CREST (Core Research for Evolutional Science and Technology) grant in the Area of High Performance Computing for Multi-scale and Multi-physics Phenomena from the Japan Science and Technology Agency (JST). The use of computational resources at the Fukui Institute for Fundamental Chemistry and at the Research Center of Computer Science (RCCS) at the Institute for Molecular Science (IMS) is acknowledged.

Supporting Information. Summary of models used to investigate the IPNS reaction. Detailed description of the computational setup and the molecular dynamics simulations. Comments on the optimization of ^{5}**7S** TS. Details of the mechanism for proton transfer in the ligand donor mechanism ^{5}**10** TS. Comparison of optimized and X-ray structures of the β-lactam intermediate and the IPN product. Structures of stationary points along the reaction pathways (in PDB format). This material is available free of charge via the Internet at http://pubs.acs.org.

References

[1] Miller, B.; Wolfenden, R. *Annu. Rev. Biochem.* **2002**, *71*, 847–885.

[2] Warshel, A.; Sharma, P. K.; Kato, M.; Xiang, Y.; Liu, H.; Olsson, M. H. M. *Chem. Rev.* **2006**, *106*, 3210–3235.

[3] Baldwin, J. E.; Bradley, M. *Chem. Rev.* **1990**, *90*, 1079–1088.

[4] Schenk, W. A. *Angew. Chem. Int. Ed.* **2000**, *39*, 3409–3411.

[5] Maseras, F.; Morokuma, K. *J. Comput. Chem.* **1995**, *16*, 1170–1179.

[6] Svensson, M.; Humbel, S.; Froese, R. D. J.; Matsubara, T.; Sieber, S.; Morokuma, K. *J. Phys. Chem.* **1996**, *100*, 19357-19363.

[7] Dapprich, S.; Komáromi, I.; Byun, K.S.; Morokuma, K.; Frisch, M. J. *J. Mol. Struct. (THEOCHEM)* **1999**, *461*, 1–23.

[8] Vreven, T.; Byun, K. S.; Komáromi, I.; Dapprich, S.; Montgomery, J. A., Jr.; Morokuma, K.; Frisch, M. J. *J. Chem. Theory Comput.* **2006**, *2*, 815–826.

[9] Lundberg, M.; Siegbahn, P. E. M.; Morokuma, K. *Biochemistry* **2008**, *47*, 1031–1042.

[10] Senn, H. M.; Thiel, W. *Top. Curr. Chem.* **2007**, *268*, 173–290.

[11] Vreven, T.; Frisch, M. J.; Kudin, K. N.; Schlegel H. B.; Morokuma, K. *Mol. Phys.* **2006**, *104*, 701–704.

[12] Vreven, T.; Morokuma, K.; Farkas, Ö.; Schlegel H. B.; Frisch, M. J. *J. Comput. Chem.* **2003**, *24*, 760-769.

[13] Prabhakar, R.; Vreven, T.; Frisch, M. J.; Morokuma, K.; Musaev, D. G. *J. Phys. Chem. B* **2006**, *110*, 13608–13613.

[14] Kwiecien, R. A.; Khavrutskii, I. V.; Musaev, D. G.; Morokuma, K.; Banerjee, R.; Paneth, P. *J. Am. Chem. Soc.* **2006**, *128*, 1287–1292.

[15] Rod, T. H.; Ryde, U. *Phys. Rev. Lett.* **2005**, *94*, 138302–(1–4).

[16] Hu, H.; Yang, W. *Annu. Rev. Phys. Chem.* **2008**, *59*, 573–601.

[17] Costas, M.; Mehn, M. P.; Jensen, M. P.; Que, L. Jr. *Chem. Rev.* **2004**, *104*, 939–986.

[18] Koehntop, K. D.; Emerson, J. P.; Que, L. Jr. *J. Biol. Inorg. Chem.* **2005**, *10*, 87–93.

[19] Bassan, A.; Blomberg, M. R. A.; Borowski, T.; Siegbahn, P. E. M. *J. Inorg. Biochem.* **2006**, *100*, 727–743.

[20] Roach, P. L.; Clifton, I. J.; Hensgens, C. M. H.; Shibata, N.; Schofield, C. J.; and Baldwin, J. E. *Nature* **1997**, *387*, 827–830.

[21] Chen, V. J.; Orville, A. M.; Harpe, M. R.; Frolik, C. A.; Surerus, K. K.; Münck, E.; Lipscomb, J. D. *J. Biol. Chem.* **1989**, *264*, 21677–21681.

[22] Brown, C. D.; Neidig, M. L.; Neibergall, M. B.; Lipscomb, J. B.; Solomon E. I. *J. Am. Chem. Soc.* **2007**, *129*, 7427–7438.

[23] Baldwin, J. E.; Bradley, M. *Chem. Rev.* **1990**, *90*, 1079–1088.

[24] Wirstam, M.; Siegbahn, P. E. M. *J. Am. Chem. Soc.* **2000**, *122*, 8539–8547.

[25] Lau, R. L.; van Eupen, J. T. H.; Schipper, D.; Tesser, G. I.; Verweij, J.; de Vroom, E. *Tetrahedron* **2000**, *56*, 7601–7606.

[26] Andersson, I.; Terwisscha van Scheltinga, A. C.; Valegård, K. *Cell. Mol. Life Sci.* **2001**, *58*, 1897–1906.

[27] Burzlaff, N. I.; Rutledge, P. J.; Clifton, I. J.; Hensgens, C. M. H.; Pickford, M.; Adlington, R. M.; Roach, P. L.; Baldwin, J. E. *Nature* **1999**, *401*, 721–724.

[28] Baldwin, J. E.; Abraham E. *Nat. Prod. Rep.* **1988**, *5*, 129–145.

[29] Becke, A. D. *J. Chem.Phys.* **1993**, *98*, 5648–5652.

[30] Lee, C.; Yang, W.; Parr, R. G. *Phys. Rev. B* **1988**, *37*, 785–789.

[31] Cornell, W. D.; Cieplak, P.; Bayly, C. I.; Gould, I. R.; Merz, K. M., Jr.; Ferguson, D. M.; Spellmeyer, D. C.; Fox, T.; Caldwell, J. W.; Kollman, P. *J. Am. Chem. Soc.* **1995**, *117*, 5179–5197.

[32] Torrent, M.; Vreven, T.; Musaev, D. G.; Morokuma, K.; Farkas, Ö.; Schlegel, H. B. *J. Am. Chem. Soc.* **2002**, *124*, 192–193.

[33] Vreven, T.; Morokuma, K. *Theo. Chem. Acc.* **2003**, *109*, 125–132.

[34] Li, J.; Cross, J. B.; Vreven, T.; Meroueh, S. O.; Mobashery, S.; Schlegel, H. B. *Proteins* **2005**, *61*, 246–257.

[35] Yoshizawa, K.; Shiota, Y. *J. Am. Chem. Soc.* **2006**, *128*, 9873–9881.

[36] Godfrey, E.; Porro, C. S.; de Visser, S. P. *J. Phys. Chem. A* **2008**, *112*, 2464–2468.

[37] Gaussian Development Version, Frisch, M. J.; Trucks, G. W.; Schlegel, H. B.; Scuseria, G. E.; Robb, M. A.; Cheeseman, J. R.; Montgomery, Jr., J. A.; Vreven, T.; Kudin, K. N.; Burant, J. C.; Millam, J. M.; Iyengar, S. S.; Tomasi, J.; Barone, V.; Mennucci, B.; Cossi, M.; Scalmani, G.;

Rega, N.; Petersson, G. A.; Nakatsuji, H.; Hada, M.; Ehara, M.; Toyota, K.; Fukuda, R.; Hasegawa, J.; Ishida, M.; Nakajima, T.; Honda, Y.; Kitao, O.; Nakai, H.; Klene, M.; Li, X.; Knox, J. E.; Hratchian, H. P.; Cross, J. B.; Bakken, V.; Adamo, C.; Jaramillo, J.; Gomperts, R.; Stratmann, R. E.; Yazyev, O.; Austin, A. J.; Cammi, R.; Pomelli, C.; Ochterski, J. W.; Ayala, P. Y.; Morokuma, K.; Voth, G. A.; Salvador, P.; Dannenberg, J. J.; Zakrzewski, V. G.; Dapprich, S.; Daniels, A. D.; Strain, M. C.; Farkas, O.; Malick, D. K.; Rabuck, A. D.; Raghavachari, K.; Foresman, J. B.; Ortiz, J. V.; Cui, Q.; Baboul, A. G.; Clifford, S.; Cioslowski, J.; Stefanov, B. B.; Liu, G.; Liashenko, A.; Piskorz, P.; Komaromi, I.; Martin, R. L.; Fox, D. J.; Keith, T.; Al-Laham, M. A.; Peng, C. Y.; Nanayakkara, A.; Challacombe, M.; Gill, P. M. W.; Johnson, B.; Chen, W.; Wong, M. W.; Gonzalez, C.; and Pople, J. A.; Gaussian, Inc., Wallingford CT, 2008.

[38] Bakowies, D.; Thiel, W. *J. Phys. Chem.* **1996**, *100*, 10580–10594.

[39] Lundberg, M.; Morokuma, K. *J. Phys. Chem. B* **2007**, *111*, 9380–9389.

[40] Altun, A.; Shaik, S.; Thiel, W. *J. Comput. Chem.* **2006**, *27*, 1324–1337.

[41] Phillips, J. C. Braun, R.; Wang, W.; Gumbart, J.; Tajkhorshid, E.; Villa, E.; Chipot, C.; Skeel, R. D.; Kale, L.; Schulten. K. *J. Comput. Chem.* **2005**, *26*, 1781–1802.

[42] Siegbahn, P. E. M. *J. Biol. Inorg. Chem.* **2006**, *11*, 695–701.

[43] Bassan, A.; Borowski, T.; Siegbahn, P. E. M. *Dalton Trans.* **2004**, *20*, 3153–3162.

[44] Kriauciunas, A.; Frolik, C. A.; Hassell, T. C.; Skatrud, P. L.; Johnson, M. G.; Holbrok, N. I.; Chen, V. J. *J. Biol. Chem.* **1991**, *266*, 11779–11788.

[45] Ogle, J. M.; Clifton, I. J.; Rutledge, P. J.; Elkins, J. M.; Burzlaff, N. I.; Adlington, R. M.; Roach, P. L.; Baldwin, J. E. *Chem. Biol.* **2001**, *8*, 1231–1237.

[46] Zheng, G.; Witek, H.; Bobadova-Parvanova, P.; Irle, S.; Musaev, D. G.; Prabhakar, R.; Morokuma, K.; Lundberg, M.; Elstner, M.; Köhler, C.; Frauenheim, T. *J. Chem. Theory Comput.* **2007**, *3*, 1349–1367.

[47] Iordanov, T.D. *J. Mol. Struct. (THEOCHEM)* **2007**, *850*, 152–159.

[48] Zheng, J. J.; Altun, A.; Thiel, W. *J. Comput. Chem.* **2007**, *28*, 2147–2158.

[49] Lundberg, M.; Blomberg, M. R. A.; Siegbahn, P. E. M. *Top. Curr. Chem.* **2004**, *238*, 79–112.

[50] Bautz, J.; Comba, P.; Lopez de Laorden, C.; Menzel, M.; Rajaraman, G. *Angew. Chem. Int. Ed.* **2007**, *46*, 8067–807.

[51] Borowski, T.; Bassan, A.; Siegbahn, P. E. M. *Inorg. Chem.* **2004**, *43*, 3277–3291.

[52] Rowe, C. J.; Shorrock, C. P. Claridge T. D. W.; Sutherland, J. D. *Chem*. *Biol*. **1998**, *5*, 229–239.

[53] Baldwin, J. E.; Adlington, R. M.; Domayne-Hayman, B. P.; Ting, H.-H.; Turner, N. J. J. Chem. Soc. Chem. Commun. **1986**, 110–113.